Lab on a Chip

PAPER

View Article Online
View Journal | View Issue

Cite this: *Lab Chip*, 2023, **23**, 3882

Programmable magnetic robot (ProMagBot) for automated nucleic acid extraction at the point of need†

Anthony J. Politza,[a] Tianyi Liu[b] and Weihua Guan *[abc]

Received 21st June 2023,
Accepted 2nd August 2023

DOI: 10.1039/d3lc00545c

rsc.li/loc

Upstream sample preparation remains the bottleneck for point-of-need nucleic acid testing due to its complexity and time-consuming nature. Sample preparation involves extracting, purifying, and concentrating nucleic acids from various matrices. These processes are critical for ensuring the accuracy and sensitivity of downstream nucleic acid amplification and detection. However, current sample preparation methods are often laboratory-based, requiring specialized equipment, trained personnel, and several hours of processing time. As a result, sample preparation often limits the speed, portability, and cost-effectiveness of point-of-need nucleic acid testing. A universal, field-deployable sample preparation device is highly desirable for this critical need and unmet challenge. Here we reported a handheld, battery-powered, reconfigurable, and field-deployable nucleic acid sample preparation device. A programmable electromagnetic actuator was developed to drive a magnetic robot (ProMagBot) in *X*/*Y* 2D space, such that various magnetic bead-based sample preparations can be readily translated from the laboratory to point-of-need settings. The control of the electromagnetic actuator requires only a 3-phase unipolar voltage in *X* and *Y* directions, and therefore, the motion space is highly scalable. We validated the ProMagBot device with a model application by extracting HIV viral RNAs from plasma samples using two widely used magnetic bead kits: ChargeSwitch and MagMAX beads. In both cases, the ProMagBot could successfully extract viral RNAs from 50 μL plasma samples containing as low as 10^2 copies of viral RNAs in 20 minutes. Our results demonstrated the ability of ProMagBot to prepare samples from complex mediums at the point of need. We believe such a device would enable rapid and robust sample preparation in various settings, including resource-limited or remote environments, and accelerate the development of next-generation point-of-need nucleic acid testing.

Introduction

Nucleic acid testing (NAT) remains the clinical standard for identifying and quantifying infectious diseases.[1–5] However, the laboratory procedures for these methods require long wait periods, trained staff, and expensive hardware to analyze the testing results.[6–8] Point-of-care (POC) devices developed over the last decades have introduced NAT in regions of need by simplifying the steps of molecular detection into compact, portable form factors.[9,10] However, the recent technological advancements motivating these devices have come in amplification assays and detection systems.[1,11,12] While these developments are significant for the future of NAT devices, a bottleneck remains with sample preparation.[7,13] Standard sample preparation methods require extensive manual processes, laboratory devices, toxic chemicals, and trained professionals.[14–16] These issues severely limit the scope of POC devices when attempting to provide quality NAT.

Sample preparation systems for laboratories depend on silica chemistry, membranes, or organic solvent methods.[17–19] These methods work well with commercial devices and trained professionals but lack simple integration for POC applications. Coated paramagnetic beads (PMBs) offer an alternative to standard techniques that is simple to integrate into portable devices.[20–22] PMBs are available with chitosan (ChargeSwitch, Invitrogen) or silica (MagMAX, Applied Biosystems) coatings designed for various sample types. Systems using these PMBs have successfully extracted and detected nucleic acids for diseases such as SARS-CoV-2,[23] HPV,[24] HIV,[25–27] RSV,[28,29] and genomic DNA.[26,30] Each PMB kit requires a specific processing protocol depending on the sample of interest and bead chemistry. Therefore, further development of universal devices that can process various PMB kits is needed.

[a] *Department of Biomedical Engineering, Pennsylvania State University, University Park 16802, USA. E-mail: wzg111@psu.edu*
[b] *Department of Electrical Engineering, Pennsylvania State University, University Park 16802, USA*
[c] *School of Electrical Engineering and Computer Science, Pennsylvania State University, University Park 16802, USA*

† Electronic supplementary information (ESI) available. See DOI: https://doi.org/10.1039/d3lc00545c

Lab-on-chip extraction systems present field-deployable methods using PMBs.[14,31–34] These systems use permanent magnets, rotational motors, and fluid pumps to manipulate magnetic bead-bound nucleic acids.[20,35–38] Lab-on-chip systems appeal to POC applications because of their small form factor, reduced volumes, and disposable components.[27,39–41] However, the microfluidic cartridges to contain these systems still require multiple manual steps and trained professionals.[30,33,39,42–44] POC diagnostics desperately need sample preparation strategies that laypersons can process, store at room temperature, and maintain during transportation.

Automated devices offer simple user interaction and have been designed for single applications. Extraction devices that process PMB kits have shown integrated permanent magnets, electromagnet (EM) controls, EM-actuated magnets, centrifuge-style rotations, automated pipetting, and fluid flow methods.[14,45–56] These methods aim to simplify the handling process for the user. However, these devices lack sample-to-extraction automation and still require intermittent manual steps.[23,30,57,58] Stationary fluid systems offer a simple format for portable devices. Devices use oil valves to separate cartridge reagents, allowing externally controlled PMBs to pass through the interfaces.[59,60] Rida *et al.* first demonstrated the ability to manipulate magnetic beads with planar coils and Chiou *et al.* demonstrated the technology's ability to process DNA.[42,50] Although movement is addressable with planar coils, these systems require high current operation and external magnetic fields. Thus, limiting the operation of these systems at the point of care.[20]Previous work by Liu *et al.* demonstrated how a permanent magnet could couple EM coils to PMB movement using low-power pulses.[49] In this manner, the need for complex external fields or high-power consumption can be eliminated. To alleviate the bottleneck of sample preparation, there is a need for devices that are fully automated, sample-agnostic, and power-efficient to process portable cartridges.

This work demonstrated a programmable, versatile, portable, and field-deployable sample preparation device. A programmable electromagnetic actuator couples a magnetic robot to paramagnetic beads (ProMagBot) in *X*/*Y* 2D space. The permanent magnet acts as a coupling device between the electromagnetic coils and the magnetic beads. Thus, ProMagBot enables magnetic bead-based extraction to be translated to the point of need. The electromagnetic actuator required a 3-phase unipolar voltage to induce *X*/*Y* 2D motion and demonstrated high scalability. The device was validated using HIV viral RNA as a model application and used two commercial magnetic bead kits: ChargeSwitch and MagMAX. ProMagBot successfully extracted viral RNAs from 50 μL plasma samples using either kit. Within 20 minutes, viral RNAs were extracted as low as 10^2 copies without wall power. These results demonstrated the ability of ProMagBot to extract nucleic acids from complex samples at the point of need. We believe such a device would enable rapid and robust sample preparation in various settings, including resource-limited or remote environments, and accelerate the development of next-generation point-of-need nucleic acid testing.

Results and discussion

Overall design

The overall design of the ProMagBot device is shown in Fig. 1a. The device contains three subcategories: A microfluidic cartridge, an electromagnetic actuator with a magnetic robot, and a computer vision system. We designed the device to control the beads from above to enhance the mixing capabilities of the cartridge (see ESI† Video S1). The electromagnetic actuator uses short pulses to attract the permanent magnet (Fig. 1c). Each coil group is repeated several times along the length of the PCB, and all are actuated simultaneously (Fig. 1b). The magnet can be moved linearly through sequential and repeated activation of the coil groups (Fig. 1d). Compared to previous magnetic coupling devices, our electromagnetic actuator design offers two large improvements.[42,49,50] ProMagBot introduces a magnetic coupling scheme that enables 2D movement with the benefit of lower energy consumption. This increases the scalability, adaptability, and portability of the device for numerous processing solutions.

System workflow

To simplify sample extraction for areas of low resources, we developed a workflow with the ProMagBot device for sample preparation (Fig. 1c). The sample of interest must first be transferred into the lysate tube containing a prepackaged lysis mixture. Then, the lysate is transferred into the microfluidic cartridge using the sample inlet. Next, the device must be powered on and the cartridge inserted into the ProMagBot device. Once the indicator lights begin flashing, the device is ready to begin the extraction process. At this step, one must press the start button to begin the process. Once finished, the device will signal that the extraction is complete using the indicator lights. Then, the cartridge can be removed from the device, and the eluted nucleic acids are contained within the elution chamber. The extraction process is fully automated and requires less than 20 min (~3–5 min of sample transfer, ~15 min of sample extraction) from sample collection to extracted nucleic acids (ESI† Video S2).

Automated sample preparation *via* microfluidic cartridge

To enable sample preparation using PMBs, we developed a microfluidic cartridge to integrate with the ProMagBot actuator. The cartridge is formed from three layers of poly(methyl methacrylate)(PMMA) that make the top layer, the microfluidic spacer, and the bottom layer (Fig. 2a). The overall layout of the cartridge can be seen in Fig. 2b. We found that 20 μL of PMB solution was required to traverse the oil valves, and most of the bead aggregate fell to the bottom of the cartridge within 1 minute. The cartridge contains a lysate chamber (100 μL), washing chamber (80 μL), and elution chamber (30 μL). Each chamber has two ports for air relief and solution injection. Air reliefs help to prevent air bubble accumulation when the cartridge is loaded. Oil valves separate the reagent chambers, providing an excellent separation method for magneto-fluidics and microfluidic cartridges.[29,48,49,61–63] We found that

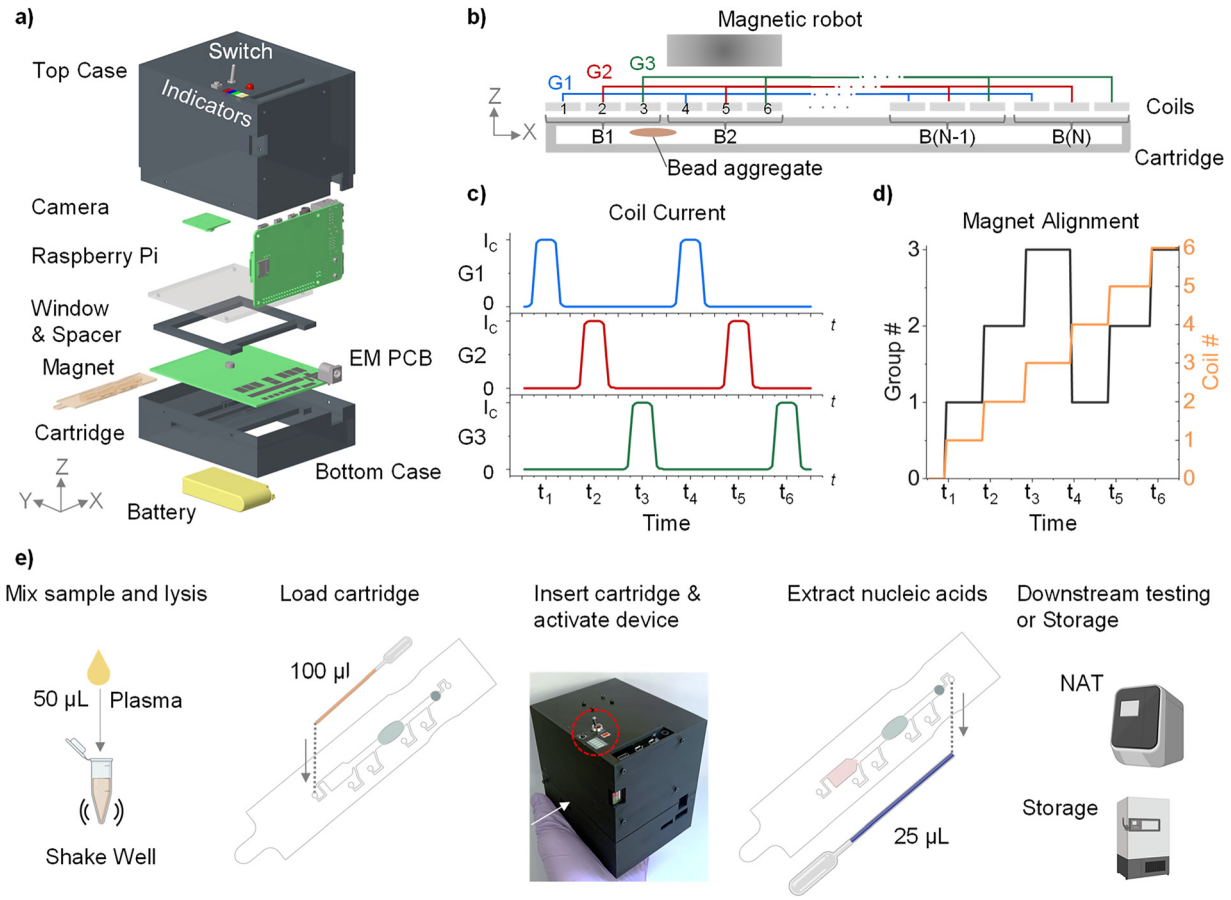

Fig. 1 Overview of the ProMagBot device, the components inside, and the necessary workflow of the system. (a) All components for the ProMagBot device are housed within a 3D-printed case (12 cm × 11.7 cm × 9.7 cm). (b) Schematic of interconnected coil groups (G1–3) and blocks (B1-N) in a cross-sectional view. (c) Current pulses through coil groups 1, 2, and 3 over time. (d) Magnet alignment during specific coil and coil group activation. (e) The ProMagBot workflow started from a 50 µL plasma sample to extracted nucleic acids.

microfluidic channel widths greater than 2 mm were best for cartridge stability and bead movement.[26,62,63] When prepackaged, the cartridge remains usable after 3–6 ft drops or after one day of commuting within a backpack (24 h.) (ESI† Fig. S1). However, our manufacturing technique limits long-term storage beyond 24 hours. The bonded layers of PMMA do not create airtight seals to prevent bubbles from forming inside the cartridge. We hypothesize that improved manufacturing technologies, such as injection molding, could quickly solve this limitation.

Fig. 2c–e demonstrates the chemical interaction occurring with the microfluidic cartridge. First, the lysis buffer adds detergents and surfactants that help break down the sample and release free nucleic acids. The low pH (<6) of the lysis buffer induces the ChargeSwitch beads with a charge that binds nucleic acids (Fig. 2c–e i). The permanent magnet can then control the PMB-nucleic acid complex and move the entire aggregate to the washing chamber. Here, the solution is neutral in pH (~7) and helps remove unwanted proteins and salts from the bead aggregate carry-over (Fig. 2c–e ii). In the elution chamber, the process reverses with a high pH (>8.5) solution. Elution reverses the binding process, releasing the nucleic acids into the solution (Fig. 2c–e iii). Once the unbound PMBs are removed, the solution contains concentrated nucleic acids that can be extracted by the user for downstream analysis.

Programmable electromagnet actuator

Scalable PCB geometry. To develop a universal electromagnetic actuator that is scalable, programmable, and compatible with PMBs, we designed our electromagnet actuator with a 3-phase unipolar voltage. The design of our PCB and coil arrangement is illustrated in Fig. 3a–c. The actuator creates 4 directions of motion ($\pm x$, $\pm y$) using six transistor switches with 3-phase unipolar voltage. The coil layout is identical for X and Y directions. A block of coils contains three separate coils belonging to a unique group (1, 2, or 3). Blocks are repeated 21 times in X and Y, while individual groups remain electrically connected. Therefore, when a group is activated, all coils are activated inside all 21 Blocks. In this manner, the permanent magnet position can always be defined as ($X_{i,j}$, $Y_{m,n}$) where X signifies the X-direction blocks and groups, i ranges from 1 to 21 (# of repeated blocks), and j represents the group number from 1 to 3. Similarly, Y signifies the Y-direction blocks and groups, where m represents the block number from 1 to 21, and n

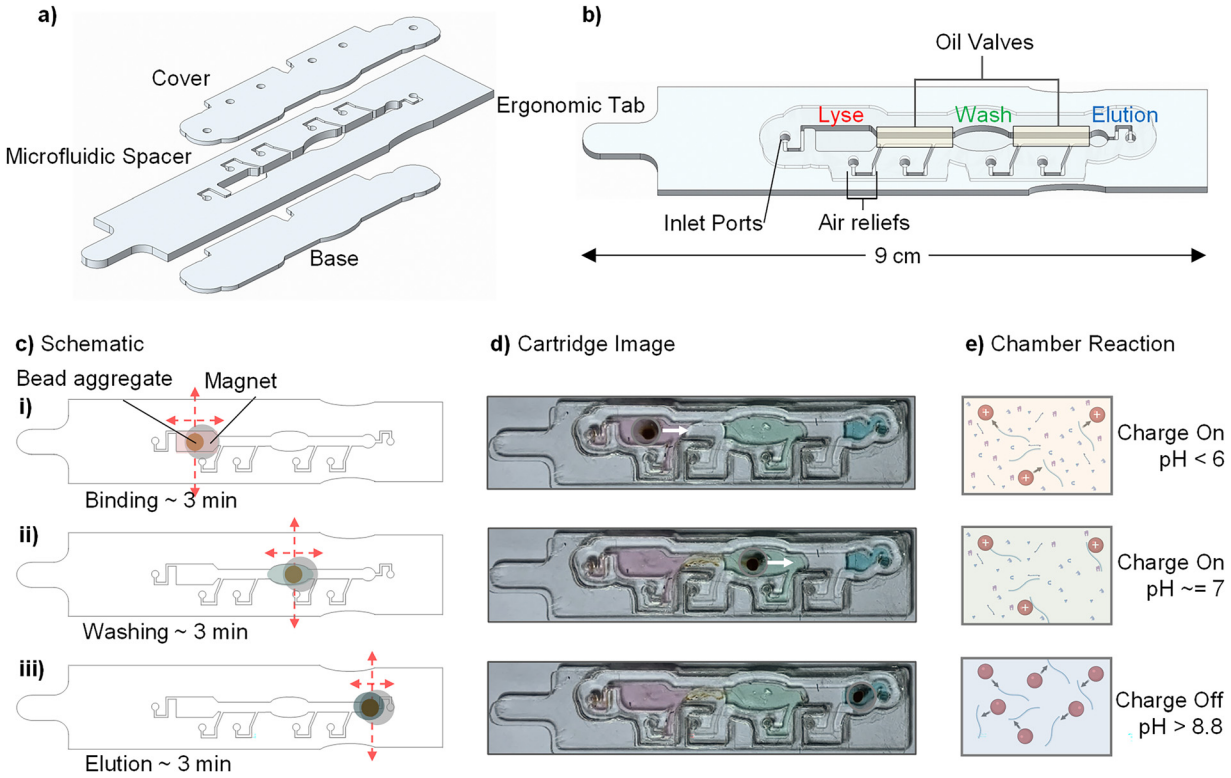

Fig. 2 Microfluidic cartridge design and features. (a) Exploded view of the cartridge's PMMA layers. (b) A top view of the cartridge displays the three-chamber structure separated by oil valves. Special air reliefs and insertion ports are located away from the main channel to prevent excess air bubbles. (i)–(iii) Three schematics of the paramagnetic bead motion and chemistry through the cartridge. (c) Schematic of magnetic robot motion and bead response. (d) Photo image of the cartridge with paramagnetic beads in each chamber. (e) Graphical representation of the Charge Switch assay. The paramagnetic beads can be bound and unbound from nucleic acids by adjusting the pH of the solution accordingly.

demonstrates the group number from 1 to 3. At a given time, along a given pathway, a block and group can define the permanent magnet in both the *X* and *Y* direction (Fig. 3a).

The permanent magnet is a coupler between the EM actuator and the PMBs. It is moved stepwise across the coil array. This style of movement is illustrated in Fig. 3b. The magnet starts aligned with coils: *X*-group-2 and *Y*-group-2. The *Y*-direction coil (*Y*-group-2) would be switched off, and the following coil (*Y*-group-3) would power on. In step 1, *X*-group-2 remains on while the *Y*-group changes, and group-3 are now powered on. Likewise, for steps 2 & 3, the *X*-group coils can be modulated identically to move the magnet along the *X*-direction. In step 3, the magnet can be moved upward to realign with *Y*-group-2. The magnet can be moved in either a positive or negative direction along those axes for both *X* and *Y* directions. This electromagnet coil array is 70 mm × 40 mm and is located on the ProMagBot PCB. Six transistor switches control the entire coil array using 3-phase unipolar voltage. The magnetic robot (permanent magnet) rests on the PCB, and the microfluidic cartridge racks underneath when installed in the case (Fig. 3c).

Magnetic field validation and control. To further evaluate our electromagnet actuator, we simulated our design using COMSOL. A 2D planar view of one plane along the magnetic coil is highlighted in Fig. 3d. We found that the distances we designed the permanent magnet to be actuated (*X* direction – red dot-dashed line: ~1 mm, *Y* direction – blue dashed line: ~0 mm) remain above a magnetic field strength of 1 mT. We also found that the field distribution across the coil length was consistent. The most vital field strength regions are noticed within the center of the coil. Each coil is ~2.6 mm wide, so we selected the closest matching disk magnet 3× the coil width so that the magnet can span three phases (6.35 mm, 0.25″, grade N52). Therefore, for any given phase, the magnet can be actuated. If we assume the permanent magnet to be in the center of a coil, we can estimate the maximum axial force (*z*-direction) experienced as:

$$B_{\text{rectangular coil}} = \frac{4\mu_0 I\sqrt{l^2+w^2}}{\pi l w} \text{ for a 4 Turn Coil}$$

$$\text{Then, } F_{\text{m}} = V_{\text{m}} \cdot M_{\text{mag}} \cdot \nabla B_{\text{coil}}$$

$$F_{\text{m}} = 8.48\times10^{-10}\left(\text{m}^3\right)\cdot 416429\left(\frac{A}{m}\right)\cdot 0.0056\left(\frac{T}{m}\right) = 0.1978 \text{ mN}$$

where F_{m} is the magnetic force on the magnet, V_{m} is the volume of the magnet, M_{mag} is the magnetization of the permanent

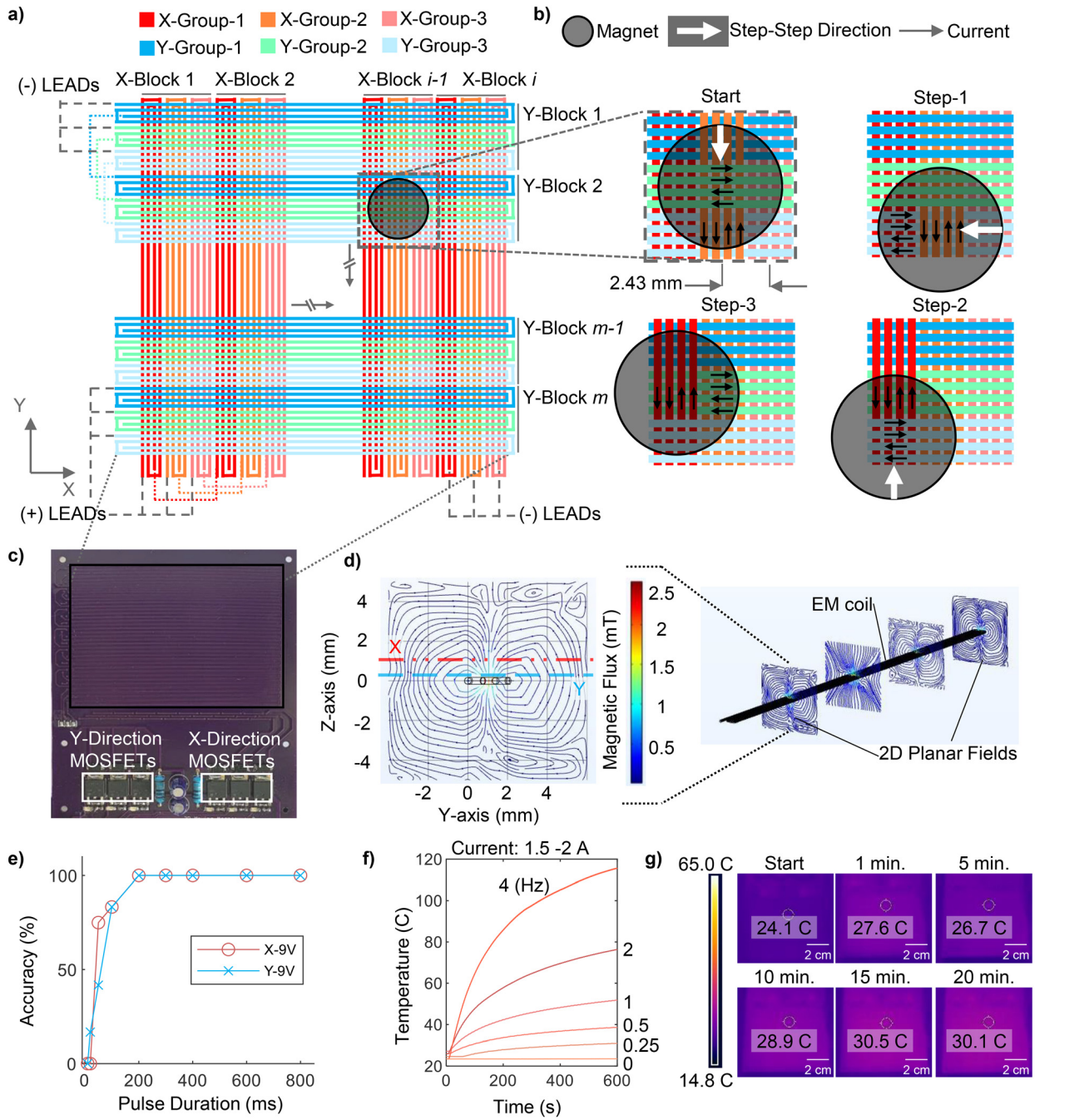

Fig. 3 Design components and considerations of the electromagnet PCB. (a) Schematic representation of the numerous electromagnet coils that are built into the PCB. These coils are defined by 21 different blocks, with each block holding three groups. Coils are activated by group designation and are interconnected across blocks. Therefore, all coils of the same group in all blocks are turned on/off together. (b) Magnet motion is achieved by turning on the next EM coil in the desired direction of motion. Motion can be achieved in any of the four cardinal directions. (c) The image of the EM PCB highlights where the actual EM coils are located. Over 50% of the PCB area is dedicated to the EM coil array. (d) 2D planar representation of the magnetic field generated by current inside one EM coil. 3D coil simulation was demonstrated through four 2D slices along the length of the coil. (e) Accuracy of the magnetic robot's motion *vs.* the length of time of activation for the EM coils in both *X* and *Y* directions. (f) The temperature of the microfluidic cartridge over time when constant EM pulses are held at various frequencies. (g) Thermal images of the PCB during an extraction protocol.

magnet (5233 Gauss), and ∇B_{coil} is the magnetic field gradient of the coil between 0 and 4 mm. All forces parallel to the coil's length will cancel out. Forces perpendicular to the coil length will be a proportion of the maximum axial force. In addition, we can approximate the magnet's acceleration under this force. With a mass of 0.754 g, the magnetic force will cause the magnet to accelerate at ~265 mm s^{-2}. We expect this force to be large enough to actuate the permanent magnet.

To test the accuracy of movement and minimize the power consumption of the ProMagBot device, we examined the

relationship between pulse duration and the accuracy of the magnetic robot. Pulse duration is defined as the time for activation of one Group of EM coils. The relationship we found can be seen in Fig. 3e. Motion in the *Y*-direction and *X*-direction demonstrate identical thresholds for when movement becomes accurate (>90%). Before this threshold of 200 ms, we observed improper movement, minor oscillations, and inactivity of the magnet. We hypothesize from our simulations and Fig. 3d that the magnetic field differences, therefore the magnetic attraction forces, affect the inertia response of the magnetic robot.

Power and thermal validation. After validating our electromagnet actuator design and movement accuracy, we examined the device's power consumption and thermal output. Peak power was recorded over a series of steps and is summarized in ESI† Fig. S2a, where all activation was kept at 1 Hz and averaged from 20 pulse commands seen in ESI† Fig. S2b & d. Peak power begins to increase from 50 ms to 200 ms, then flatlines at approximately 20 W per pulse. Therefore, we can minimize our power consumption and maximize accuracy by using a pulse duration of 200 ms for both *X* and *Y* directions. Consequently, for a 20 W pulse lasting 200 ms, we expect one motion step to use 1.11 mW h (4 Joules). We found that the device consumed 1.21 Wh per extraction (~15 min). Thus, the entire ProMagBot device can be powered by a 1600 mAh (14.4 Wh) LiPo battery for eight extractions.

We designed the electromagnetic actuator to be universal and scalable. However, adding coil lengths beyond the microfluidic channel width could introduce heat harmful to the samples of interest. We recorded the cartridge temperature during 10 minutes of constant coil activation for pulses of 200 ms at frequencies from 0 to 4 Hz. The cartridge temperature can reach above 70 °C when the device is operated at 2 Hz and higher. However, when operated under 0.5 Hz, the cartridge temperature does not climb above 40 °C Fig. 3f. ESI† Fig. S3a–f shows each *X* and *Y* coil after activation for 5 s. These images show the precise thermal distribution and geometry of the EM coils. Even within the 5 s power cycle, the temperature of the EM actuator does not exceed 40 °C. Therefore, with a pulse length of 200 ms, the rest time between pulses should be 300 ms. Next, we examined the temperature of the PCB and cartridge during a mock extraction protocol. As shown in Fig. 3g, the PCB temperature increases over the 20 min runtime, but the temperature does not exceed 31 °C. With the device closed, the cartridge temperature, during a mock extraction protocol, never reached above 34 °C (ESI† Fig. S3g).

Pathway automation and feedback control

After developing our electromagnet actuator, we included a feedback system to enable scalable and controllable 2D motion. Our electromagnet actuator's design allows all directions of motion to be controlled through six transistor switches; however, at any given time for any given coil, there are multiple instances where our magnet could rest. To add feedback for the ProMagBot device, we added a camera inside the device that monitors the magnet's real-time positioning after each step. The software block diagram is illustrated in Fig. 4a. Once a programmed pathway is added to the device (series of selected points), the device will automatically move the magnet to those points in serial order.

Three pathways were generated to demonstrate the camera and electromagnet actuator integration. These pathways, seen in Fig. 4b–d, exaggerate movement in the four cardinal directions as proof of motion for the device. The numbers designate the point location and order, while the colored lines track the magnet during movement. Fig. 4b shows a pathway mimicking a sine wave propagating along the $+X$ direction. Fig. 4c demonstrates a sine wave propagating along the $-Y$ direction, and Fig. 4d defines a combination of the two prior pathways. The timelapse of each pathway can be seen in ESI† Video S3, where it is clear to visualize the magnetic robot movement in all directions. Thus, our demonstration of controlled and programmable motion in 2D space presents a novel approach to magnetofluid manipulation that offers redundancy and scalability compared to previous methods.[35,48–50,52]

Performance evaluation using mock HIV samples

To demonstrate the performance of the ProMagBot device and microfluidic cartridge, we validated the system with spiked samples of HIV viral RNA into EDTA buffer (ethylenediaminetetraacetic acid) and healthy human plasma. ChargeSwitch RNA extraction from the contrived buffer and plasma samples was operated by the ProMagBot device. Following extraction, all samples were immediately frozen at −80 °C for later testing by RT-qPCR. Contrived samples were generated by spiking 10^5 to 10^0 copies of purified HIV RNA into 50 μL of either sample type (2000 down to 0.02 copies per μL). Fig. 5a shows the real-time qPCR results for the plasma samples. Positive samples are identified when the curve reaches an RFU threshold greater than the mean plus three standard deviations ($\mu + 3\sigma$). At this threshold a Cq value can be defined, where samples with an input concentration above 10^2 were detected from EDTA buffer (2 cp μL^{-1}) and 10^3 from healthy plasma (20 cp μL^{-1}) (Fig. 5b). These results show a ~10% decrease in extraction performance for plasma samples, while both samples demonstrated strong linearity across detectable concentrations (R = 0.99). Therefore, the quantitative threshold for our system shows a limit of extraction (100%) of 10^2 and 10^3 copies for buffer and plasma samples respectively (ESI† Fig. S6). Lower extraction performance from plasma is expected as it contains debris, gDNA, nucleases, and other inhibitors compared to EDTA buffer. The entire cartridge extraction can be visualized in ESI† Video S4.

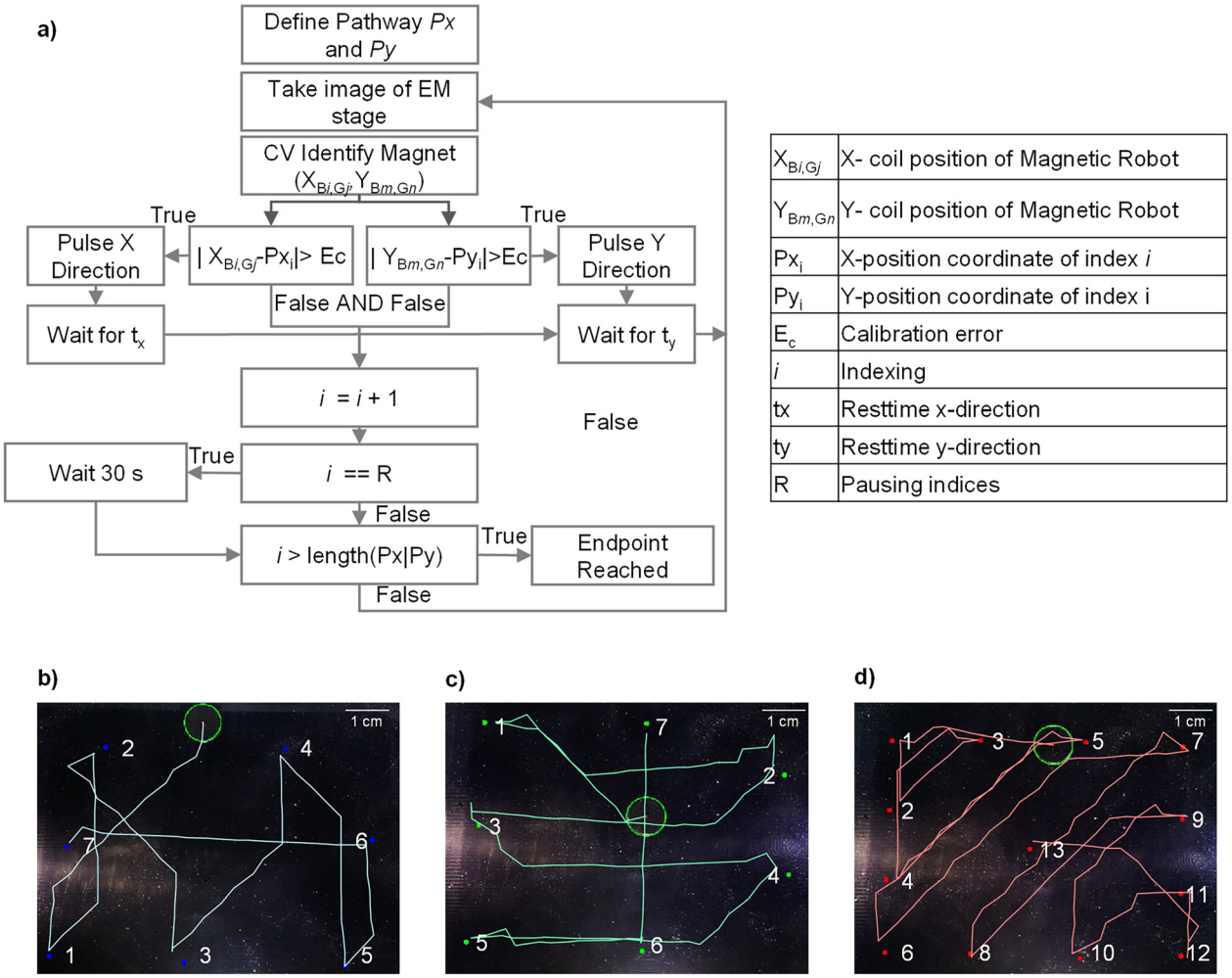

$X_{Bi,Gj}$	X- coil position of Magnetic Robot
$Y_{Bm,Gn}$	Y- coil position of Magnetic Robot
Px_i	X-position coordinate of index *i*
Py_i	Y-position coordinate of index i
E_c	Calibration error
i	Indexing
tx	Resttime x-direction
ty	Resttime y-direction
R	Pausing indices

Fig. 4 Magnetic robot motion control *via* the camera vision algorithm. (a) Block diagram explaining the logic flow through the camera vision algorithm for magnetic robot movement. The input to the algorithm is an image of the magnet stage inside the device. From there, the algorithm detects the location of the magnetic robot, compares the location, and activates the appropriate EM coils to move the magnet in the direction needed to reach the set point. (b–d) Photo images of the EM PCB overlayed with the movement pathway of the magnetic robot for the numbered pathway. The magnetic robot can be moved in any of the four cardinal directions, accurately follow a pathway, and track various pathways.

The PCR samples were verified using gel electrophoresis to validate our extraction performance. In Fig. 5c, the gel shows DNA bands with identical results to our PCR analysis, where detection is absent in samples containing 10^2 input copies. The amplicon band is visible at 79 bp, and the primers (forward and reverse) and probes can be distinguished as minor, less intense bands, respectively.[64] We are confident the detection assay worked as intended from these results, and the extraction procedure is compatible with downstream PCR analysis.

We integrated the MagMAX PMB assay into our design to increase the universal application of the ProMagBot device and improve plasma extraction. Fig. 5d shows the real-time results for the samples that were detected. Samples as low as 10^2 input copies of purified RNA (2 cp μL^{-1} sample) were detected with qRT-PCR. Plasma samples showed decreased linearity (R^2 = 0.55) and consistency compared to spiked buffer samples (R^2 =0.83) (Fig. 5e). A degradation in consistency was expected as the integration of the MagMAX kit was not fully compatible with our cartridge fabrication techniques. The required ethanol and isopropanol for the MagMAX kit reacted poorly with our PMMA cartridges, and the recommended extraction protocol had to be modified. However, the MagMAX kit improved the lower limit of extraction from plasma samples (10^2 copies). Gel electrophoresis showed similar results to the ChargeSwitch kit, where amplicon bands can be seen for all samples (Fig. 5f). Increased smearing in these images was expected with carrier RNA (unknown length), genomic DNA, or protein carry-over. With improvements to our cartridge techniques (inert materials, seamless fabrication), we expect the performance of the MagMAX kit could be significantly improved. We found the system's efficiency was relatively low with both extraction kits (see ESI† Fig. S5). We suspect our performance is related to oil interfaces that cause RNA to be ripped off from the bead aggregate, RNA is adsorbed to the

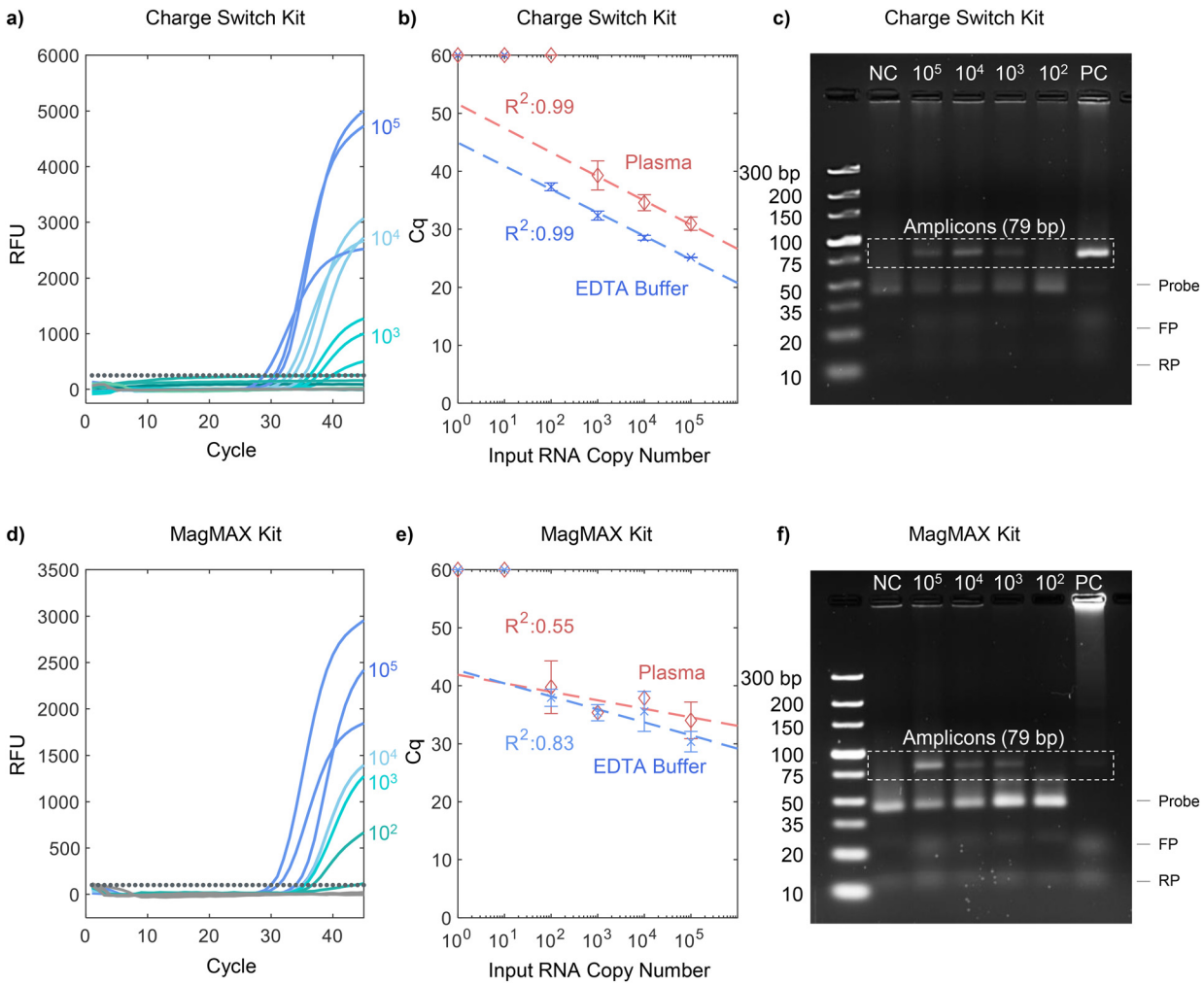

Fig. 5 Plasma extraction performance using the ProMagBot device and protocol. (a) Amplification curves for triplicate testing (N = 3) of purified RNA extraction from 50 μL plasma samples using the ChargeSwitch kit. RFU threshold = $\mu + 3\sigma$. (b) Input copy number *vs.* Cq value from PCR analysis. The limit of extraction using the Charge Switch kit is 1000 (plasma) and 100 (buffer) copies. Negative samples are demonstrated as Cq = 60. (c) Gel-electrophoresis image of Charge Switch extracted RNA samples after PCR amplification. (d) Amplification curves for triplicate testing (N = 3) of purified RNA extraction from 50 μL plasma samples using the MagMAX kit. RFU threshold = $\mu + 3\sigma$. (e) Input copy number *vs.* Cq value from qRT-PCR analysis. The limit of extraction using MagMAX is 100 copies for buffer samples. Negative samples are demonstrated as Cq = 60. (f) Gel-electrophoresis of MagMAX extracted RNA samples after PCR amplification. Gel notes: the high contrast amplicon band occurs at 79 bp. Faint bands at the bottom of the gel show the PCR forward (FP) and reverse (RP) primers and TaqMan-style probes. Positive-control (PC) and negative-control (NC) wells show the presence and absence of an amplicon band, respectively. The positive control loading well shows large or blocked products in this image. The blockage could be caused using a 5% gel by (1) high concentration samples, (2) enzyme-bound DNA, (3) excess amplified sample, or (4) other high molecular weight debris.

hydrophilic surfaces of PMMA, or the reduction of extraction reagents beyond the recommended amount. For future development of extraction devices, we plan to explore these areas to improve extraction efficiency and other extraction technologies, such as silica matrices and spin columns.

Conclusion

Sample preparation remains the most significant bottleneck for point-of-need nucleic acid testing due to its complexity and time-consuming nature. We demonstrated a fully integrated device for rapid (<20 min) sample preparation of HIV RNA from plasma samples. Sample extraction was conducted using a 3-phase unipolar electromagnetic actuator, automated by the ProMagBot device. This portable and automatic system is compatible with two commercial bead kits and demonstrates the scalability and versatility of our novel actuator design. To simplify the device, we plan to evaluate multiplex processing and explore alternative feedback technologies. To improve extraction performance, we will further investigate magnetic bead handling techniques inside microfluidic cartridges. Overall, ProMagBot validated viral RNA extraction as low as 10^2 copies from 50 μL of plasma (2 cp μL^{-1}) within 20 minutes and without wall power. Device extraction showed strong linearity (R^2 = 0.99) in qRT-PCR analysis. These results demonstrate the ability of

ProMagBot to prepare samples from complex mediums at the point of care. We believe such a device would enable rapid and robust sample preparation in various settings for numerous diseases to accelerate the development of next-generation point-of-need testing.

Materials and methods

Microfluidic cartridge

Inside the microfluidic cartridge, there are 4 separate components. Three main chambers contain the lysate, washing buffer, and elution buffer. The lysate is mixed and loaded from the user. The following reagents80 (μL) of washing buffer), oil valves and 30 (μL) an elution buffer, can be preloaded into the cartridge sequentially using the inlet ports. The last remaining component is mineral oil (80 μL × 2) to separate the chambers (Millipore Sigma, USA). The cartridge comprises three stacked layers: base, channel spacer, and cover. These layers are 1/32″, 1/16″, and 1/32″ thick, respectively, of polymethyl methacrylate (PMMA), purchased from **https://Inventables.com**. These layers are designed using Creo Parametric (PTC, Boston, MA) and then laser-cut using a VLS3.60DT from Universal Laser Systems (Scottsdale, AZ). The three separate layers are bonded using an acrylic solvent and treated under UV light for 60 minutes for disinfection. All reagents and materials used are detailed in ESI† Table S1.

Cartridge adjustments for MagMAX kit

The MagMAX cartridge holds the same footprint as the original microfluidic cartridge, with channel width and lysis chamber size modifications. The channel width was increased from 2 mm to 3 mm, and the lysis chamber was increased to hold 150 μL of lysate. All other design and fabrication methods are identical to the original cartridge.

ProMagBot device and EM PCB

All components of the ProMagBot device are housed within a 3D-printed case made of ABS plastic (k = ~0.18 W m^{-1} K^{-1}). The 3D printer and ABS material are sourced from MakerBot (MakerBot Industries LLC, New York City, NY). The case (ABS), spacers (ABS), and viewing windows (PMMA, k = ~0.21 W m^{-1} K^{-1}) were modeled using Creo Parametric. The customized EM PCB and control board were designed in AutoCAD Eagle (Autodesk Inc.) and fabricated by OSH Park LLC (Portland, OR) (see ESI† Fig. S6). The magnetic robot is a N52 cylindrical magnet (0.25″ diameter and 0.125″ thickness) from K&J Magnets (Pipersville, PA). All other electronic components: indication LEDs, push buttons, switches, or connectors, were purchased from Digi-Key (Thief River Falls, MN) (ESI† Table S2). The LiPo battery, XT60 connector, and JST-XH connectors were purchased from Hobby King (Kwun Tong, Hong Kong). The 9 V 6A Power Supply used to connect the ProMagBot device to a wall outlet was purchased from Amazon (Seattle, WA). The Raspberry Pi 4 and Pi Camera module v2 were purchased from Cana Kit (North Vancouver, Canada).

Computer vision

Computer vision and magnetic robot tracking use a Raspberry Pi camera module v2 paired with a Raspberry Pi 4. The module is mounted 3.5 in. away from the magnetic robot and stage. The stage is illuminated by three 120-degree, wide-angle LEDs illuminating the device's viewing window. A custom Python script automates image capture and magnetic robot detection on the Pi 4.

COMSOL simulation

Magnetic field simulations were run within COMSOL 2020 (COMSOL Inc.). Our model was adapted from the stock *Electromagnetic coil simulation*, and the geometry of our PCB coil was imported into the software. The current was set to 1.5 A, and the boundary around the coil was defined as a 2 cm × 2 cm × 7 cm rectangular prism.

Automated extraction

To prepare the ProMagBot device for automated extraction, an extraction pathway was calibrated to match the permanent magnet and magnetic beads. Pathway calibration was conducted manually on the Raspberry Pi and is only required once for each cartridge geometry. Once complete, the pathway is saved in a .csv file that the device references for all the following extractions.

Plasma extraction

Healthy plasma samples (Research Blood Components, Watertown, MA) were first pretreated with 1 μL of proteinase K (Invitrogen, Waltham, MA) and incubated at 60 °C for 15 minutes. Each 50 μL sample was spiked with viral RNA (HIV-1 Subtype B, Sera Care Life Science, Milford, MA) from 10^5 to 10^0 copies. The plasma sample was then combined with a premixed solution of ChargeSwitch beads (10 μL), Lysis Buffer (20 μL), and Binding Buffer (19 μL), all from the ChargeSwitch Total RNA Extraction Kit (Invitrogen, Waltham, MA). Once combined, the 100 μL was inserted into the lysis chamber of the microfluidic cartridge. All air inlets on the cartridge were pre-sealed with tape, and the cartridge can be inserted into the ProMagBot device for automated extraction.

When using the MagMAX extraction kit (Applied Biosystems, Waltham, MA), the lysis chamber volume included 20 μL of MagMAX beads, 10 μL of binding enhancer, 34 μL of lysis buffer, 34 μL of isopropyl alcohol (70%), and 2 μL of carrier RNA. The washing chamber used the ChargeSwitch Wash, and the elution chamber held 30 μL of MagMAX elution buffer.

RT-qPCR assay

The procedure and reagents followed the PCR HIV assay validated by Palmer *et al.* (Supplementary Table S3).[64] From

30 μL of elution buffer, 10 μL was used as the RNA sample for PCR analysis. Therefore, our total PCR volume consisted of 25 μL: 6.25 μL of Fast Taq One-Step Master Mix (Applied Biosystems, Waltham, MA), 1.5 μL of Forward and Reverse primer, 0.63 μL of Probe, 10 μL of extracted RNA sample, and 5.13 μL of Nuclease-free water (New England Biolabs, Ipswich, MA). Testing was performed on a Bio-Rad C1000 Thermal Cycler (Hercules, CA). Thermal Cycling was set as 50 °C for 5 min, 95 °C for 3 s, 65 °C for 30s, and repeated 45×.[64] Primers and probes were purchased from Integrated DNA Technologies (Coralville, IA). Positive samples were identified from the background RFU by a threshold of $\mu + 3\sigma$.

Gel electrophoresis

Gel electrophoresis was completed using an agarose gel of 5% wt. Gel was made using agarose powder, and 50X TBE buffer spiked with SYBR Safe Stain (Invitrogen, Waltham, MA) and cured for 45 min. The DNA ladder was Thermofisher's Ultra Low DNA Ladder (Waltham, MA). Each gel lane was loaded with a 15 μL mixture of PCR and loading buffer with a ratio of 5 : 1. The voltage was 110 V, and the gel ran for 50 minutes before imaging on Bio-Rad's GelDoc Go (Hercules, CA).

Data analysis method and statistics

All statistical analysis and regression modeling was completed using MATLAB R2020 (Natick, MA). All plots showing data demonstrate mean and 3 standard deviations for triplicate testing unless otherwise noted. All data processing used MATLAB. All figures and plots were created with MATLAB and PowerPoint.

Associated content

The ESI† includes microfluidic cartridge durability testing, device power consumption, device thermal distributions, cartridge and device bill of materials, the qRT-PCR primer set, demonstrations of Mag-On-Top magnetic mixing, the ProMagBot extraction protocol, pathway tracking in 2D space, and pathway and bead response during extractions.

Author contributions

Anthony J. Politza: conceptualization, software, investigation, writing – original draft. Tianyi Liu: conceptualization, resources, writing – review & editing. Weihua Guan: conceptualization, writing – review & editing, project administration, and funding acquisition.

Conflicts of interest

Weihua Guan, Anthony J. Politza, and Tianyi Liu have a provisional patent application for the technology disclosed herein.

Acknowledgements

This work was partially supported by the National Science Foundation (1902503, 1912410, 2045169) and the National Institute of Health (R61AI147419, R33HD105610) and USDA grant # 2023-70432-39480. Any opinions, findings, conclusions, or recommendations expressed in this work are those of the authors and do not necessarily reflect the views of the National Science Foundation and the National Institutes of Health.

References

1 P. Craw and W. Balachandran, *Lab Chip*, 2012, **12**, 2469–2486.
2 I. M. Mackay, K. E. Arden and A. Nitsche, *Nucleic Acids Res.*, 2002, **30**, 1292–1305.
3 I. M. Mackay, *Clin. Microbiol. Infect.*, 2004, **10**, 190–212.
4 W. M. Freeman, S. J. Walker and K. E. Vrana, *BioTechniques*, 1999, **26**, 112–125.
5 N. R. Blumenfeld, M. A. E. Bolene, M. Jaspan, A. G. Ayers, S. Zarrandikoetxea, J. Freudman, N. Shah, A. M. Tolwani, Y. Hu and T. L. Chern, *Nat. Nanotechnol.*, 2022, **17**, 984–992.
6 M. N. Esbin, O. N. Whitney, S. Chong, A. Maurer, X. Darzacq and R. Tjian, *RNA*, 2020, **26**, 771–783.
7 A. Niemz, T. M. Ferguson and D. S. Boyle, *Trends Biotechnol.*, 2011, **29**, 240–250.
8 W. S. Stevens and T. M. Marshall, *J. Infect. Dis.*, 2010, **201**, S78–S84.
9 S. Ceffa, R. Luhanga, M. Andreotti, D. Brambilla, F. Erba, H. Jere, S. Mancinelli, M. Giuliano, L. Palombi and M. C. Marazzi, *J. Virol. Methods*, 2016, **229**, 35–39.
10 E. Guichet, L. Serrano, C. Laurent, S. Eymard-Duvernay, C. Kuaban, L. Vidal, E. Delaporte, E. M. Ngole, A. Ayouba and M. Peeters, *J. Virol. Methods*, 2018, **251**, 75–79.
11 Y. Manmana, T. Kubo and K. Otsuka, *TrAC, Trends Anal. Chem.*, 2021, **135**, 116160.
12 Y. Zhao, F. Chen, Q. Li, L. Wang and C. Fan, *Chem. Rev.*, 2015, **115**, 12491–12545.
13 S. Soni and B. J. Toley, *Sens. Actuators, B*, 2021, 131272.
14 J. Park, D. H. Han and J.-K. Park, *Lab Chip*, 2020, **20**, 1191–1203.
15 S. R. Jangam, A. K. Agarwal, K. Sur and D. M. Kelso, *Biosens. Bioelectron.*, 2013, **42**, 69–75.
16 M. A. Dineva, L. Mahilum-Tapay and H. Lee, *Analyst*, 2007, **132**, 1193–1199.
17 M. L. Cunha, S. S. da Silva, M. C. Stracke, D. L. Zanette, M. N. Aoki and L. Blanes, *Anal. Chem.*, 2021, **94**, 41–58.
18 F. Tian, C. Liu, J. Deng, Z. Han, L. Zhang, Q. Chen and J. Sun, *Sci. China: Chem.*, 2020, **63**, 1498–1506.
19 L. Zhang, F. Tian, C. Liu, Q. Feng, T. Ma, Z. Zhao, T. Li, X. Jiang and J. Sun, *Lab Chip*, 2018, **18**, 610–619.
20 Y. Zhang and N.-T. Nguyen, *Lab Chip*, 2017, **17**, 994–1008.
21 S. Berensmeier, *Appl. Microbiol. Biotechnol.*, 2006, **73**, 495–504.
22 R.-J. Yang, H.-H. Hou, Y.-N. Wang and L.-M. Fu, *Sens. Actuators, B*, 2016, **224**, 1–15.

23 J. Kang, Y. Li, Y. Zhao, Y. Wang, C. Ma and C. Shi, *Anal. Biochem.*, 2021, **635**, 114445.
24 L. Zhang, R. N. Deraney and A. Tripathi, *Biomicrofluidics*, 2015, **9**, 064118.
25 S. M. Berry, A. J. LaVanway, H. M. Pezzi, D. J. Guckenberger, M. A. Anderson, J. M. Loeb and D. J. Beebe, *J. Mol. Diagn.*, 2014, **16**, 297–304.
26 K. Sur, S. M. McFall, E. T. Yeh, S. R. Jangam, M. A. Hayden, S. D. Stroupe and D. M. Kelso, *J. Mol. Diagn.*, 2010, **12**, 620–628.
27 J. Zhang, X. Su, J. Xu, J. Wang, J. Zeng, C. Li, W. Chen, T. Li, X. Min and D. Zhang, *Biomicrofluidics*, 2019, **13**, 034102.
28 N. M. Adams, H. Bordelon, K.-K. A. Wang, L. E. Albert, D. W. Wright and F. R. Haselton, *ACS Appl. Mater. Interfaces*, 2015, **7**, 6062–6069.
29 H. Bordelon, N. M. Adams, A. S. Klemm, P. K. Russ, J. V. Williams, H. K. Talbot, D. W. Wright and F. R. Haselton, *ACS Appl. Mater. Interfaces*, 2011, **3**, 2161–2168.
30 H. Bordelon, P. K. Russ, D. W. Wright and F. R. Haselton, *PLoS One*, 2013, **8**, e68369.
31 C. H. Ahn, J.-W. Choi, G. Beaucage, J. H. Nevin, J.-B. Lee, A. Puntambekar and J. Y. Lee, *Proc. IEEE*, 2004, **92**, 154–173.
32 K. A. Hagan, C. R. Reedy, M. L. Uchimoto, D. Basu, D. A. Engel and J. P. Landers, *Lab Chip*, 2011, **11**, 957–961.
33 C.-J. Liu, K.-Y. Lien, C.-Y. Weng, J.-W. Shin, T.-Y. Chang and G.-B. Lee, *Biomed. Microdevices*, 2009, **11**, 339–350.
34 R. H. Liu, J. Yang, R. Lenigk, J. Bonanno and P. Grodzinski, *Anal. Chem.*, 2004, **76**, 1824–1831.
35 G. Choi, D. Song, S. Shrestha, J. Miao, L. Cui and W. Guan, *Lab Chip*, 2016, **16**, 4341–4349.
36 A. Dehghan, A. Gholizadeh, M. Navidbakhsh, H. Sadeghi and E. Pishbin, *Sens. Actuators, B*, 2022, **351**, 130919.
37 M. Shikida, K. Takayanagi, K. Inouchi, H. Honda and K. Sato, *Sens. Actuators, B*, 2006, **113**, 563–569.
38 J. Wang, K. Morabito, T. Erkers and A. Tripathi, *Analyst*, 2013, **138**, 6573–6581.
39 X. Shi, C.-H. Chen, W. Gao, S.-H. Chao and D. R. Meldrum, *Lab Chip*, 2015, **15**, 1059–1065.
40 C.-H. Wang, K.-Y. Lien, J.-J. Wu and G.-B. Lee, *Lab Chip*, 2011, **11**, 1521–1531.
41 J.-H. Wang, L. Cheng, C.-H. Wang, W.-S. Ling, S.-W. Wang and G.-B. Lee, *Biosens. Bioelectron.*, 2013, **41**, 484–491.
42 C.-H. Chiou, D. J. Shin, Y. Zhang and T.-H. Wang, *Biosens. Bioelectron.*, 2013, **50**, 91–99.
43 Y. Zhang, S. Park, K. Liu, J. Tsuan, S. Yang and T.-H. Wang, *Lab Chip*, 2011, **11**, 398–406.
44 A. Y. Trick, F.-E. Chen, L. Chen, P.-W. Lee, A. C. Hasnain, H. H. Mostafa, K. C. Carroll and T.-H. Wang, *medRxiv*, 2021, preprint, DOI: **10.1101/2021.05.10.21256995**.
45 S. M. Azimi, G. Nixon, J. Ahern and W. Balachandran, *Microfluid. Nanofluid.*, 2011, **11**, 157–165.
46 L. Becherer, J. F. Hess, S. Frischmann, M. Bakheit, H. Nitschko, S. Stinco, F. Zitz, H. Hofer, G. Porro and F. Hausladen, *Micromachines*, 2021, **12**, 159.
47 A. Y. Trick, H. T. Ngo, A. H. Nambiar, M. M. Morakis, F.-E. Chen, L. Chen, K. Hsieh and T.-H. Wang, *Lab Chip*, 2022, **22**, 945–953.
48 G. Choi, T. Prince, J. Miao, L. Cui and W. Guan, *Biosens. Bioelectron.*, 2018, **115**, 83–90.
49 T. Liu, G. Choi, Z. Tang, A. Kshirsagar, A. J. Politza and W. Guan, *Biosens. Bioelectron.*, 2022, **209**, 114255.
50 A. Rida, V. Fernandez and M. A. M. Gijs, *Appl. Phys. Lett.*, 2003, **83**, 2396–2398.
51 W. Jung, J. Han, J.-W. Choi and C. H. Ahn, *Microelectron. Eng.*, 2015, **132**, 46–57.
52 A. Y. Trick, J. H. Melendez, F.-E. Chen, L. Chen, A. Onzia, A. Zawedde, E. Nakku-Joloba, P. Kyambadde, E. Mande and J. Matovu, *Sci. Transl. Med.*, 2021, **13**, eabf6356.
53 F. Hu, J. Li, Z. Zhang, M. Li, S. Zhao, Z. Li and N. Peng, *Anal. Chem.*, 2019, **92**, 2258–2265.
54 S. Witt, J. Neumann, H. Zierdt, G. Gébel and C. Röscheisen, *Forensic Sci. Int.: Genet.*, 2012, **6**, 539–547.
55 K. Kadimisetty, J. Song, A. M. Doto, Y. Hwang, J. Peng, M. G. Mauk, F. D. Bushman, R. Gross, J. N. Jarvis and C. Liu, *Biosens. Bioelectron.*, 2018, **109**, 156–163.
56 L. Van Heirstraeten, P. Spang, C. Schwind, K. S. Drese, M. Ritzi-Lehnert, B. Nieto, M. Camps, B. Landgraf, F. Guasch and A. H. Corbera, *Lab Chip*, 2014, **14**, 1519–1526.
57 F.-E. Chen, P.-W. Lee, A. Y. Trick, J. S. Park, L. Chen, K. Shah, H. Mostafa, K. C. Carroll, K. Hsieh and T.-H. Wang, *Biosens. Bioelectron.*, 2021, **190**, 113390.
58 S. Byrnes, A. Fan, J. Trueb, F. Jareczek, M. Mazzochette, A. Sharon, A. F. Sauer-Budge and C. M. Klapperich, *Anal. Methods*, 2013, **5**, 3177–3184.
59 H. T. Ngo, M. Jin, A. Y. Trick, F.-E. Chen, L. Chen, K. Hsieh and T.-H. Wang, *Anal. Chem.*, 2022, **95**, 1159–1168.
60 A. Beyzavi and N.-T. Nguyen, *J. Phys. D: Appl. Phys.*, 2008, **42**, 015004.
61 N. M. Adams, A. E. Creecy, C. E. Majors, B. A. Wariso, P. A. Short, D. W. Wright and F. R. Haselton, *Biomicrofluidics*, 2013, **7**, 014104.
62 Z. Long, A. M. Shetty, M. J. Solomon and R. G. Larson, *Lab Chip*, 2009, **9**, 1567–1575.
63 D. Troiano, R. N. Deraney and A. Tripathi, *Colloids Surf., A*, 2017, **513**, 188–195.
64 S. Palmer, A. P. Wiegand, F. Maldarelli, H. Bazmi, J. M. Mican, M. Polis, R. L. Dewar, A. Planta, S. Liu and J. A. Metcalf, *J. Clin. Microbiol.*, 2003, **41**, 4531–4536.